Lipid bilayer coated Al_2O_3 nanopore sensors: towards a hybrid biological solid-state nanopore

Bala Murali Venkatesan · James Polans ·
Jeffrey Comer · Supriya Sridhar · David Wendell ·
Aleksei Aksimentiev · Rashid Bashir

Abstract Solid-state nanopore sensors are highly versatile platforms for the rapid, label-free electrical detection and analysis of single molecules, applicable to next generation DNA sequencing. The versatility of this technology allows for both large scale device integration and interfacing with biological systems. Here we report on the development of a hybrid biological solid-state nanopore platform that incorporates a highly mobile lipid bilayer on a single solid-state Al_2O_3 nanopore sensor, for the potential reconstitution of ion channels and biological nanopores. Such a system seeks to combine the superior electrical, thermal, and mechanical stability of Al_2O_3 solid-state nanopores with the chemical specificity of biological nanopores. Bilayers on Al_2O_3 exhibit higher diffusivity than those formed on TiO_2 and SiO_2 substrates, attributed to the presence of a thick hydration layer on Al_2O_3, a key requirement to preserving the biological functionality of reconstituted membrane proteins. Molecular dynamics simulations demonstrate that the electrostatic repulsion between the dipole of the DOPC headgroup and the positively charged Al_2O_3 surface may be responsible for the enhanced thickness of this hydration layer. Lipid bilayer coated Al_2O_3 nanopore sensors exhibit excellent electrical properties and enhanced mechanical stability ($G\Omega$ seals for over 50 h), making this technology ideal for use in ion channel electrophysiology, the screening of ion channel active drugs and future integration with biological nanopores such as α-hemolysin and MspA for rapid single molecule DNA sequencing. This technology can find broad application in bio-nanotechnology.

B. M. Venkatesan · J. Polans · S. Sridhar · R. Bashir
Department of Electrical and Computer Engineering,
University of Illinois at Urbana Champaign,
Illinois, IL 61801, USA

B. M. Venkatesan · J. Polans · S. Sridhar · R. Bashir
Micro and Nanotechnology Laboratory,
University of Illinois at Urbana Champaign,
Illinois, IL 61801, USA

J. Comer · A. Aksimentiev · R. Bashir
Department of Physics,
University of Illinois at Urbana Champaign,
Illinois, IL 61801, USA

J. Comer · A. Aksimentiev
Beckman Institute, University of Illinois at Urbana Champaign,
Illinois, IL 61801, USA

R. Bashir (✉)
Department of Bioengineering,
University of Illinois at Urbana Champaign,
Illinois, IL 61801, USA
e-mail: rbashir@illinois.edu

D. Wendell
College of Medicine, University of Cincinnati,
Cincinnati, OH 45221, USA

D. Wendell
College of Engineering, University of Cincinnati,
Cincinnati, OH 45221, USA

1 Introduction

Biological membranes form the physical barrier between the interior of cells and their extracellular environments and play an important role in cellular structure and function. These membranes consist of a variety of integral and peripheral membrane proteins (receptors, transporters, ion channels, pumps, lipid metabolic enzymes, nuclear porins) and carbohydrates embedded in a fluid lipid bilayer matrix, the interactions of these membrane proteins with their environment facilitating vital cellular processes such as membrane trafficking and intracellular signaling. The ability of membrane proteins to regulate cellular activity also makes them an ideal target for drug development, with cell membrane receptors, largely G protein-coupled receptors and enzymes, accounting for over 70% of all current drug targets (Drews 2000).

The functional role of membrane proteins is typically investigated using supported phospholipid bilayers (SPBs), an *in-vitro* analog to the biological cell membrane. SPBs are continuous lipid membranes formed on hydrophilic substrates containing a 10–20 Å trapped interfacial water layer, essential to preserving the long range fluidity and functionality of the bilayer (Koenig et al. 1996; Castellana and Cremer 2006). SPBs have been used to study cell-cell interactions (Sackmann 1996; Grakoui et al. 1999), cell growth and adhesion (Groves et al. 2001), multivalent receptor-ligand binding (Shi et al. 2007), controlled drug release (Mager and Melosh 2008), and also find application in electro optical biosensors, drug discovery and biocatalysis (Sackmann 1996). In addition, these model biomimetic systems are mechanically more robust than freestanding black lipid membranes (BLMs) and can be integrated with surface specific analytical techniques such as atomic force microscopy (AFM) and nuclear magnetic resonance (NMR).

The two most common techniques to form SPBs on hydrophilic substrates are the Langmuir-Blodgett transfer technique (Solletti et al. 1996), and the vesicle adsorption and rupture method (Cremer and Boxer 1999; Reimhult et al. 2003). The latter is more versatile, allows for the incorporation of membrane proteins during vesicle preparation and has been traditionally used to form SPBs on quartz (Johnson et al. 1991), glass (Cremer and Boxer 1999), mica (Raedler et al. 1995) and metal oxides such as TiO$_2$ and SrTiO$_3$ (Starr and Thompson 2000). The vesicle rupture process is highly dependent on surface electrostatics (Cha et al. 2006) and van der Waals forces (Reimhult et al. 2002). High adhesion energies result in vesicle rupture,

bilayer stiction and a loss of lateral fluidity, as seen with bilayers formed on chromium and indium tin oxide substrates (Groves et al. 1998), making these SPBs incompatible with membrane protein integration. In contrast, low surface adhesion energy on substrates such as Al$_2$O$_3$ prevents vesicle rupture from occurring resulting in intact, stable supported vesicle layers (SVLs) (Nollert et al. 1995; Mager et al. 2008). A variety of strategies have been used to increase surface adhesion energy to induce bilayer formation on Al$_2$O$_3$ including surface functionalization (Roskamp et al. 2008), preparation of charged lipid compositions (Drexler and Steinem 2003), and the addition of fusigenic agents such as polyethylene glycol (Berquand et al. 2003). These strategies however require additional processing steps, chemically modify the surface characteristics of Al$_2$O$_3$ and potentially mask the desired optical and electrical properties of the substrate.

Here, we report the formation of highly fluid, defect free lipid bilayers on unmodified Al$_2$O$_3$ surfaces through vesicle fusion and apply this technique to form high impedance, fluid lipid bilayers on single Al$_2$O$_3$ nanopore sensors. Solid-state nanopores are emerging as next generation bionanosensors for the electrical detection, analysis, and manipulation of single biomolecules, particularly DNA, RNA and small proteins. The electrical detection of target molecules through these solid-state pores is typically done using two-terminal electrophoresis, resulting in characteristic blockades in the measured ionic current. This technique has been used to probe various biophysical phenomena at the single molecule level including unzipping kinetics of hairpin DNA (McNally et al. 2008; Zhao et al. 2008), stretching transitions in dsDNA (Heng et al. 2005), biomolecule folding (Li et al. 2003), DNA sizing and sieving (Storm et al. 2005), DNA counterion condensation and saturation (Chang et al. 2006), and the detection of DNA-protein complexes (Smeets et al. 2008). More recently, we demonstrated the development of mechanically stable nanopores in Al$_2$O$_3$ for the sensitive detection and analysis of individual DNA molecules (Venkatesan et al. 2009; Venkatesan et al. 2010). These sensors exhibit exceptional electrical noise performance and an inherent ability to electrostatically reduce DNA transport rates, a fundamental requirement for nanopore based, electronic DNA sequencing. Suspending fluid lipid bilayers on these Al$_2$O$_3$ solid-state sensors opens up new possibilities, allowing for the reconstitution of single ion channels, the sensitive screening of ion channel active drugs, and the insertion of chemically selective biological nanopore channels such as α-hemolysin and MspA for DNA sequencing. Proteinaceous mutant α-hemolysin and MspA nanopores are currently capable of discriminating individual nucleotides, making way for a single molecule sequencing approach (Clarke et al. 2009; Derrington et al.

2010). The use of these biological nanopores as commercial diagnostic sensors however, is limited by the lack of mechanical stability of the lipid membranes into which they are inserted. Biointerfacing highly sensitive, mechanically stable Al_2O_3 nanopores with fluid lipid bilayers for protein channel insertion provides a robust solution, an important first step in the development of hybrid biological solid-state nanopores, applicable to medical diagnostics, drug screening and DNA sequencing.

We demonstrate first the formation of fluid lipid bilayers on planar atomic layer deposited (ALD) Al_2O_3 surfaces, a material system previously deemed incompatible with bilayer formation. Vesicle rupture on Al_2O_3 occurs exclusively in the presence of high osmotic pressure and Ca^{2+}, resulting in bilayers that exhibit significantly higher lateral fluidity than those formed on planar SiO_2 and TiO_2 substrates. Molecular dynamics simulations show an association of the lateral fluidity with an enhanced separation between the DOPC bilayer and the Al_2O_3 surface, and furthermore attribute this phenomenon to electrostatic repulsion between the lipid headgroup and the positively charged Al_2O_3 surface. Bilayer formation on single Al_2O_3 nanopores prevented ion transport through the pore, resulting in a $G\Omega$ seal comparable in impedance to that of conventional BLMs. In addition, bilayer coated Al_2O_3 nanopores were stable in ionic solution for in excess of 50 h, significantly more stable than BLMs (typical lifetime 6–10 h). These results confirm that a positively charged Al_2O_3 solid-state nanopore interface is well suited for the formation of high impedance, highly mobile, mechanically stable lipid bilayers for potential biointegration with chemically sensitive protein channels.

2 Materials and methods

2.1 Materials

The lipids used in these experiments were 1,2-di-(9Z-octadecenoyl)-sn-glycero-3-phosphocholine (DOPC) purchased, dissolved in chloroform, from Avanti. Polar Lipids (Alabaster, AL) and Texas Red dihexadecanoyl-phosphoethanolamine (TR-DHPE), purchased from Invitrogen (California, USA) in the anhydrous power form. An alternative fluorescent lipid was also used in experiments, 1-palmitoyl-2-6-[(7-nitro-2-1,3-benzoxadiazol-4-yl)amino]hexanoyl-sn-glycero-3-phosphocholine (NBD-PC), also purchased, dissolved in chloroform, from Avanti Polar Lipids (Alabaster, AL). Unless otherwise noted, all experiments were conducted in buffer solutions consisting of 1 M KCl, 10 mM Tris-base, 5 mM $CaCl_2$ or 1 M KCl, 10 mM Tris-base, 5 mM EDTA adjusted to pH 8.0 using NaOH. High purity, deionized water (18 MΩ.cm) from a

MilliPore MilliQ system (Bedford, MA) was used in all experiments.

2.2 Vesicle and surface preparation

Large unilamellar vesicles were prepared using the following protocol. Briefly, DOPC in chloroform was mixed with 1 mol% TR-DHPE and dried under a steady stream of N_2, followed by overnight desiccation under vacuum to remove any excess chloroform. Lipids were then hydrated in DI water at 4 C to a final concentration of 1 mg/ml. The large multilammelar vesicles obtained were extruded 31 times through a 400 nm pore size polycarbonate membrane filter (Avanti Mini-Extruder from Avanti Polar Lipids). Where stated, 1 mol% NBD-PC fluorescent lipid was substituted in place of 1 mol% TR-DHPE in certain vesicle preparations. Vesicles were generally used within 1–3 days of preparation.

Planar Al_2O_3 surfaces were prepared by first cleaning glass cover slips (Corning) in 1:1 H_2SO_4:H_2O_2 for 15 min followed by atomic layer deposition of 200Å of Al_2O_3 using a Cambridge Nanotech Savannah 200 reactor operated at 250°C. TiO_2 surfaces were prepared using the same cleaning process followed by deposition of 250Å of TiO_2 using a Lesker PVD 75 sputter system at an RF power of 300 W at 25°C. SiO_2 surfaces were used as is. The material composition of these surfaces was confirmed using X-ray photoelectron spectroscopy (XPS) as shown in the supplementary material. Surface roughness and surface uniformity was studied using AFM, also shown in the supplementary material.

2.3 Vesicle fusion and bilayer formation

Prior to vesicle fusion, all surfaces were treated in a 100 W O_2 plasma for 1 min to render the surfaces hydrophilic and immediately bonded to a PDMS microfluidic channel with a volume of 9 μl. A schematic of the experimental setup is shown in the supplementary material. Within 20 min of the O_2 surface treatment, vesicles were introduced into the microfluidic system and incubated on the various surfaces for 2 h at room temperature. Following incubation, a 10 min DI rinse at a flow rate of 5 μl/min was used to remove any excess vesicles and surface debris resulting in the presence of high density SVLs on Al_2O_3 and TiO_2 surfaces. To transition SVLs on planar Al_2O_3 and TiO_2 to SPBs, a 10 min perfusion using 1 M KCl, 10 mM Tris, 5 mM $CaCl_2$, pH 8.0 buffer at a high flow rate of 10 μl/min was used resulting in the formation of highly fluid bilayers on all surfaces examined. Excess Ca^{2+} following bilayer formation was removed by rinsing with 1 M KCl, 10 mM Tris-base, 5 mM EDTA, pH 8.0. This same process was used to form fluid lipid bilayers on Al_2O_3 nanopore sensors.

2.4 Fluorescence Recovery After Photobleaching (FRAP)

Fluorescence imaging and FRAP measurements were conducted on a Zeiss LSM 710 Multiphoton Confocal Microscope equipped with a 561 nm 2 mW laser. Diffusion coefficients were determined by momentarily bleaching a spot of diameter ~50 μm containing fluorescently labeled lipids using a laser beam from a 2.5 W mixed gas Ar+/Kr + laser (Stabilite 2018, Spectra Physics). Samples were irradiated at 568.2 nm with 100 mW of power for several seconds. The photobleached spot was measured as a function of time using time-lapse imaging and subsequently processed using Zen 2008 and ImageJ software. The fluorescence intensity of the bleached spot was determined after background subtraction and normalization. Using the method of Kapitza with minor corrections for the finite bleach time (Kapitza et al. 1985), the diffusion coefficient of the dye-labeled lipids on the various surfaces examined were determined.

2.5 Nanopore fabrication

The nanopore fabrication process has been described in detail previously (Venkatesan et al. 2009; Venkatesan et al. 2010). ALD was used to deposit 500Å of Al_2O_3 onto a double-sided polished <100> silicon wafer at a platen temperature of 250°C using tetramethylaluminum (TMA) as the metal precursor and water vapor as the oxygen precursor. Next, photolithography was used to pattern 30 μm square openings on the wafer backside. The patterned photoresist (AZ9260) layer defined the mask for the following backside deep Si trench etch. 300 μm deep, high-aspect ratio (10:1) trenches were formed on the wafer backside using the Bosch process. 495 such etch/passivation cycles were required to etch completely through the 300 μm thick Si handle layer and to stop on the Al_2O_3 membrane layer. Free standing Al_2O_3 membranes of thickness 45±5 nm were formed using this process. Nanopores of varying diameter were formed in these membranes using a focused electron beam from a JEOL JEM2010F field-emission TEM operated at 197 kV in convergent beam electron diffraction (CBED) mode. Larger 200 nm nanopores in 45±5 nm thick Al_2O_3 membranes were formed using a FEI DB235 focused ion beam (FIB) tool at a beam current of 30 pA.

2.6 Molecular dynamics simulations

Atomic scale models of four solid-state membranes, having surface charge densities of −1, 0, +1, or +2 e/nm^2 and each containing a nanopore, were created by the methods described in the supplementary information. To neutralize the −1, +1, and +2 e/nm^2 surfaces, 280 K^+ ions, 280 Cl^- ions, and 560 Cl^- ions, respectively, were added within 0.5 nm of the surfaces. Subsequently, a lipid bilayer consisting of 292 DOPC lipids was added to fill the xy plane above each of the four differently charged solid-state surfaces; the headgroups of the lipids in the nearest leaflet of bilayer were on average separated from the surfaces by 1.0 nm. The solid-state membrane and lipids were then immersed in 1.0 M KCl solution to form complete systems of ~220,000 atoms, which each measured about 23.2 nm along the direction normal to the solid surfaces after equilibration at 1 atm of pressure.

Following energy minimization, the four systems were then simulated using NAMD (Phillips et al. 2005) with a 2 fs timestep, multiple timestepping, particle-mesh Ewald electrostatics (Batcho et al. 2001), and periodic boundary conditions along all three axes. The SETTLE algorithm (Miyamoto and Kollman 1992) was used to enforce the rigidity of water molecules; the RATTLE algorithm (Andersen 1983) enforced rigidity of all other covalent bonds involving hydrogen atoms. Interactions among the lipids, water, and ions were computed using the CHARMM27 force field (MacKerell et al. 1998). The interactions between atoms of the system and the silicon and oxygen atoms of the membrane were calculated using the force field of Cruz-Chu et al. (Cruz-Chu et al. 2006), except that the charges of some oxygen atoms were modified as discussed in the supplementary information. Lennard-Jones interactions and explicit pairwise electrostatic forces were computed with a smooth 0.7–0.8 nm cutoff. The pressure was maintained at 1 atm using a Nosé–Hoover Langevin piston pressure control (Martyna et al. 1994); the temperature was maintained at 295 K by applying a Langevin thermostat (damping constant of 1 ps^{-1}) to the atoms of the solid-state membrane only. To maintain the area per lipid at 0.72 nm^2, the pressure control modified the system size only along the z direction (Siu et al. 2008). Lipid diffusivity calculations are described in the supplementary material.

3 Results and discussion

3.1 Bilayer formation on Al_2O_3 surfaces

Lipid bilayers were formed on planar Al_2O_3 surfaces through the fusion and rupture of 400 nm extruded DOPC vesicles containing 1 mol% Texas Red DHPE fluorescently labeled lipid. Vesicles were formed by rehydration of a lipid cake in DI water as described in the materials and methods section. Figure 1a is a schematic of the microfluidic setup used in these experiments. Surfaces were O_2 plasma treated for 1 min at 100 W prior to vesicle incubation with surface hydrophilicity being confirmed
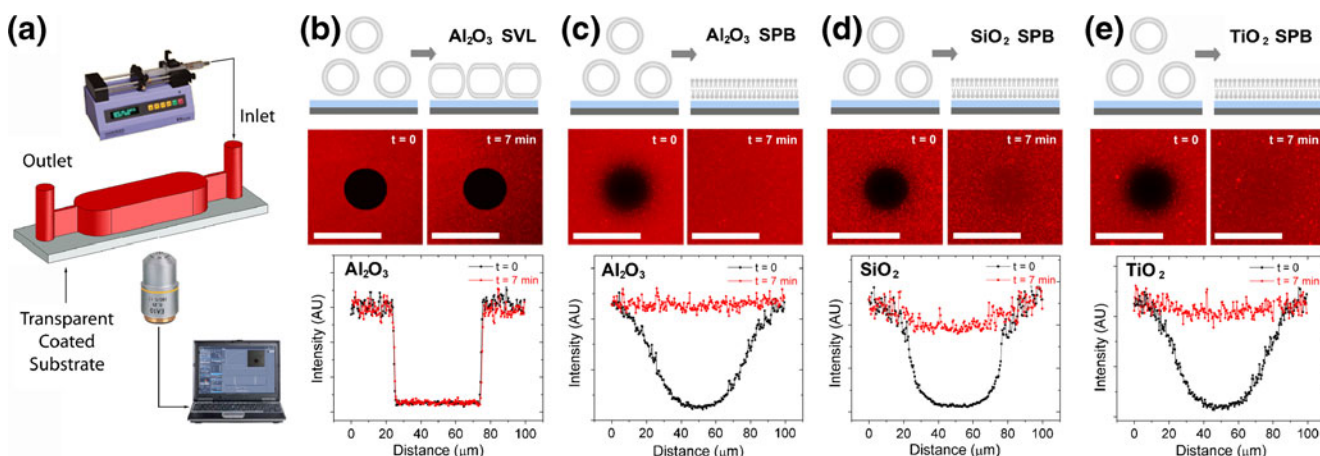
Fig. 1 (**a**) Schematic of the experimental setup showing the micro-fluidic channel bonded to planar, coated, transparent substrates mounted on a confocal microscope (**b**) Vesicle fusion on planar Al_2O_3 surfaces in the presence of DI water only. A 50 μm spot was photobleached and then reimaged 7 min later. The fluorescence intensity profile at $t=0$ and $t=7$ min shows no fluorescence recovery, consistent with the formation of an immobile SVL (**c**) Vesicle rupture on planar Al_2O_3 surfaces in the presence of high salt (1 M KCl, 10 mM Tris, pH 8.0) and Ca^{2+}. Clear fluorescence recovery is observed in the photobleached region after 7 min confirming that osmotic pressure and Ca^{2+} induce the formation of a fluid, supported phospholipid bilayer (SPB) on Al_2O_3 (**d**) Fluorescence recovery on a control SiO_2 surface in the presence of high salt and Ca^{2+} (**e**) Fluorescence recovery on a control TiO_2 surface in the presence of high salt and Ca^{2+}, again confirming the formation of a SPB. Scale bars in (**b**)–(**e**) are 100 μm

through contact angle measurements (supplementary material). The incubation of vesicles on planar Al_2O_3 surfaces in the presence of DI water alone resulted in the formation of high density, immobile SVLs confirmed by the lack of fluorescence recovery seen in the photobleached spot (Fig. 1b) in fluorescence recovery after photobleaching (FRAP) experiments (Axelrod et al. 1976). This result is consistent with previous reports that suggest Al_2O_3 is incompatible with bilayer formation due to low vesicle-substrate adhesion energy, resulting in the formation of intact, stable SVLs (Nollert et al. 1995; Mager et al. 2008). To induce the formation of fluid lipid bilayers on Al_2O_3 following vesicle incubation, surfaces were perfused in a 1 M KCl, 10 mM Tris, 5 mM $CaCl_2$, pH 8.0 solution followed by a 1 M KCl, 10 mM Tris, 5 mM EDTA, pH 8.0 solution to remove any excess Ca^{2+} (flow rates of 10 μl/min). The presence of DI inside the vesicle versus high ionic strength solution outside (1 M KCl) induced an osmotic gradient across the vesicle membrane. Osmotic pressure and the presence of Ca^{2+} in turn induced the transition of a high density SVL on Al_2O_3 to a highly fluid lipid bilayer as shown in the line profiles of Fig. 1c. Ca^{2+} is known to bridge the negatively charged phosphate groups in DOPC (Richter et al. 2003), whilst accelerating vesicle adsorption on metal oxide surfaces (Csucs and Ramsden 1998). Osmotic pressure has also been reported to cause compressive stress and vesicle deformation, resulting in stress induced rupture and bilayer formation (Reimhult et al. 2003). Fluorescence recovery as a function of time on Al_2O_3 is illustrated in supplementary figure 1a.

To ensure that the transition from SVL to SPB on Al_2O_3 was not due to electrostatic interactions between Ca^{2+} and the net negatively charged fluorescent lipid used in these experiments (1% TR-DHPE in DOPC vesicles), we replaced TR-DHPE with a zwitterionic fluorescent lipid molecule (NBD-PC) and the formation of highly mobile lipid bilayers on Al_2O_3 was still observed as seen in supplementary figure 1b. The bilayer formation process reported here was also tested on planar SiO_2 and TiO_2 control surfaces as seen in Fig. 1d and e respectively, again resulting in the formation of highly fluid bilayers. These results confirm that although surface-lipid adhesion alone is insufficient to directly induce vesicle rupture on Al_2O_3, this material does indeed support fluid lipid bilayers in the presence of osmotic pressure and Ca^{2+}.

3.2 Lipid diffusion kinetics on planar surfaces

The diffusion kinetics of lipids in SPBs is a strong indicator of surface hydration. The presence of a 1–3 nm thick interfacial aqueous layer is essential to maintaining the functionality of membrane proteins, particularly transporters. For this reason, the kinetics of lipid diffusion on planar Al_2O_3, TiO_2, SiO_2 and PDMS surfaces was investigated using quantitative FRAP analysis. Figure 2a presents typical fluorescence recovery curves from DOPC bilayers formed on each surface, the fastest recovery being observed on Al_2O_3 and the slowest recovery on SiO_2. The diffusion coefficients of the dye-labeled lipid in each case was extracted by fitting a single exponential to each curve in accordance with the method of Kapitza (Kapitza et al.
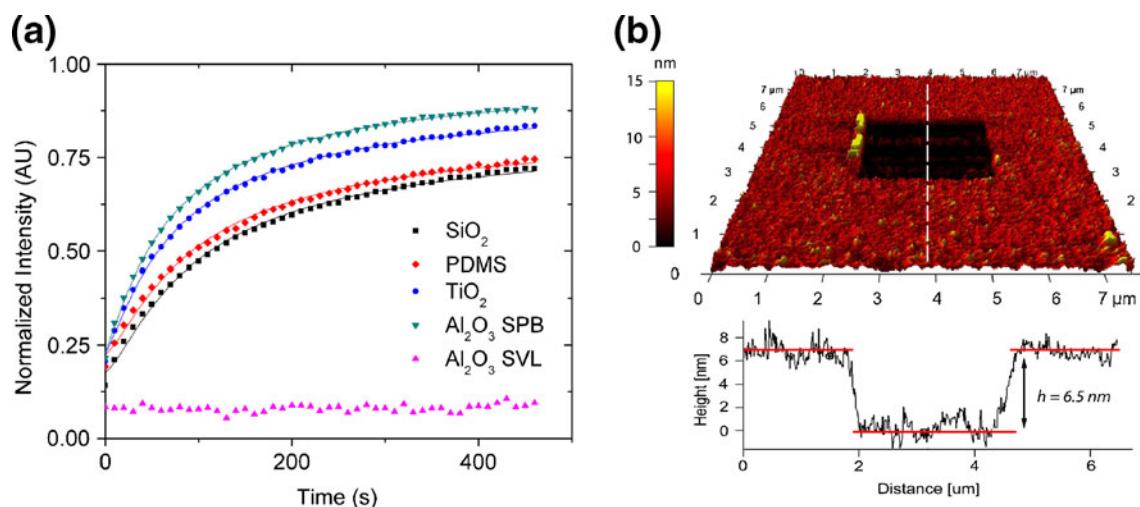
Fig. 2 (a) Typical FRAP curves from DOPC bilayers formed on SiO₂, PDMS, TiO₂ and Al₂O₃ substrates in the presence of high salt and Ca²⁺. Quantitative FRAP analysis shows faster recovery on Al₂O₃. Data is fitted using the theoretical Kapitza model (shown by the *solid lines*), with diffusion coefficients and fit residuals given in Table 1 (b) Typical DOPC bilayer step height after bilayer formation

on Al₂O₃, imaged using fluid AFM technique. A 2.5×2.5 μm region was scribed in the bilayer under high force (>50 nN) using a SiN tip and then reimaged in tapping mode. Line profile through the scribed region gave a step height of 6.5 ± 1 nm, confirming the formation of a single DOPC bilayer

1985) (see materials and methods). Lipid diffusion coefficients, fit error, *rms* surface roughness, and water contact angle were measured for each substrate and are summarized in Table 1. The results of Table 1 confirm that lipid diffusivity is highest on Al₂O₃, followed by TiO₂, PDMS and SiO₂. The measured diffusion coefficients of 2.4 μm²/s and 1.75 μm²/s for TiO₂ and SiO₂ respectively are consistent with reported values of 2.5 μm²/s on TiO₂ (Starr and Thompson 2000)(Starr and Thompson 2000) and 1.4–2.0 μm²/s on SiO₂ (Mager et al. 2008). Interestingly, lipid diffusivity on Al₂O₃ was significantly higher. This enhanced diffusivity is likely dependent on a combination of factors including surface topography, material composition, surface hydration and surface electrostatics (Cassier et al. 1999; Mager et al. 2008). These parameters were investigated systematically.

To examine the role of surface topography, AFM was conducted (supplementary figure 2a) on each surface and revealed a significantly higher *rms* surface roughness for TiO₂ versus Al₂O₃ and SiO₂ substrates. Little correlation between surface roughness and lipid diffusion kinetics was observed. The material composition of all surfaces was verified using x-ray photoelectron spectroscopy (XPS) as shown in supplementary figure 2b, thereby ruling out the influence of surface contamination on lipid diffusion dynamics. To examine macroscopic differences in surface hydration, water contact angle measurements were conducted on bare substrates after an O₂ plasma treatment (1 min at 100 W). The hydrophilicity of each substrate was similar (<5° in all cases as shown in supplementary figure 2c). Microscopic differences in DOPC bilayer thickness on Al₂O₃ versus SiO₂ was probed using fluid AFM. Post bilayer formation on Al₂O₃, a 2.5 μm square region in the bilayer was scribed in contact mode under high force (>50 nN), sufficient to scrape through the bilayer as demonstrated by Kumar et al. (Kumar and Hoh 2000). The area encapsulating the scribed region was then reimaged at low force in tapping mode resulting in the AFM scan shown in Fig. 2b. A line profile through the scribed region revealed a step height of 6.5 ± 1 nm, corresponding to the thickness of a single bilayer. DOPC bilayers formed on Si₃N₄ and Mica typically exhibit thicknesses of 4.6 nm (Kataoka-Hamai et al. 2008) and 5.6 nm (Leonenko et al. 2002) respectively, confirmed through fluid AFM studies. The increased DOPC bilayer thickness on Al₂O₃ suggests the possible presence of a thicker hydration layer. NMR studies using phosphatidyl-

Table 1 Summary of results showing the rms roughness and water contact angle, θ, on planar Al₂O₃, SiO₂, TiO₂ and PDMS surfaces. Also shown are the diffusion coefficients of TR-DHPE fluorescent lipid in DOPC bilayers formed on these surfaces. The method of Kapitza was used for data fitting with R² fit values as shown

	Al₂O₃	SiO₂	TiO₂	PDMS
rms roughness (pm)	241	152.2	941	–
θ (deg)	<5°	<5°	<5°	<5°
D (μm²/s)	2.7	1.75	2.4	1.8
R²	0.999	0.996	0.998	0.996

choline lipids in anodic aluminum oxide (AAO) templates confirmed the existence of a substantially thick, 3 nm trapped water layer between the bilayer and the alumina substrate,(Gaede et al. 2004) in comparison to the 1 nm hydration layer typically reported on SiO_2 (Groves et al. 1997). It is likely that this thick hydration layer reduces lipid-substrate interactions, resulting in the enhanced bilayer fluidity observed on Al_2O_3. Note, these AFM height measurements also exclude the possibility of stacked bilayers on Al_2O_3 which typically result in step heights of >10 nm (Koenig et al. 1996).

3.3 The influence of surface charge

To examine the role of surface electrostatics on surface hydration, a series of molecular dynamics simulations were carried out. The simulation protocols are described in detail in the experimental methods; the general methodology is reviewed by (Aksimentiev 2010). Briefly, an atomistic model of an amorphous solid-state membrane was created, which contained a nanopore to permit the passage of water and ions in and out of the interfacial water layer. Surfaces of differing

charge densities (-1, 0, $+1$, and $+2$ e/nm^2) were generated by shifting the charge on oxygen atoms at the membrane surface. This ensured that the positions of atoms of the solid-state surface were identical in all simulations, thereby eliminating the effects of surface roughness whilst probing only electrostatic effects. The simulated charge densities were consistent with reported values for SiO_2 and Al_2O_3. Hydrated SiO_2 surfaces typically exhibit a surface charge density of -1 e/nm^2 at pH 8.0 due to the deprotonation of surface silanol groups (White et al. 2006), in contrast to ALD Al_2O_3 surfaces which have been shown to carry a positive charge under similar conditions with charge densities in excess of $+1$ e/nm^2 (Adiga et al. 2007). The four complete systems, each consisting of a DOPC bilayer, water, ions, and a solid-state membrane containing a nanopore, were simulated to observe the evolution of both the DOPC bilayer and the interfacial water layer as a function of time.

Figure 3a illustrates the position of the DOPC bilayer relative to the solid-state membrane at various time points during the simulation for the negatively charged (-1 e/nm^2) and positively charged ($+2$ e/nm^2) surfaces. An initial lipid-
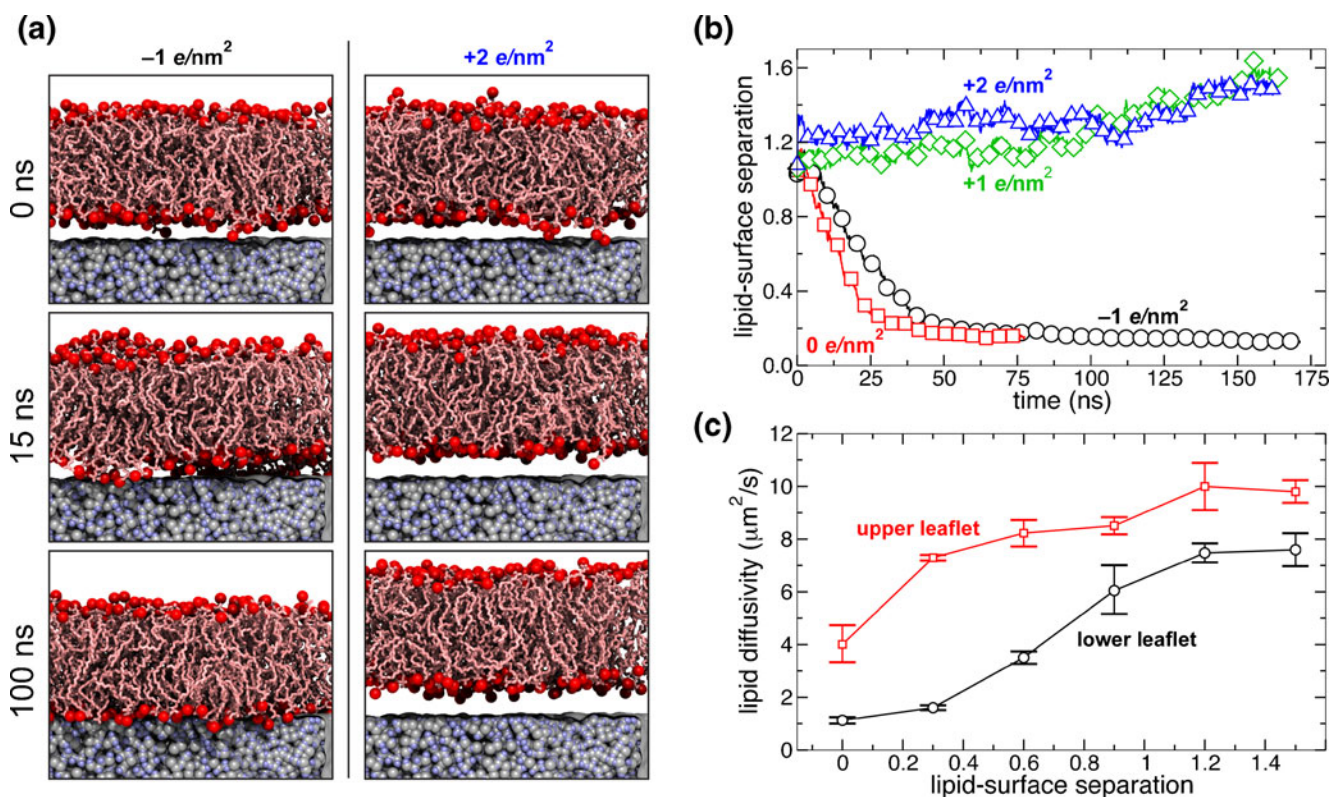

Fig. 3 Molecular dynamics simulations of the interaction between a DOPC bilayer and solid-state surfaces of varying surface charge densities. (**a**) Snapshots illustrating the position of the DOPC bilayer over a negatively (*left*) and positively (*right*) charged surface at various time points during molecular dynamics simulations. The complete system contained a bilayer with a lateral area of 105 nm^2, only a portion is shown in these snapshots. The choline groups are shown as red spheres; the rest of the DOPC molecules are drawn as pink tubes. The atoms of the synthetic membrane are shown by gray and blue spheres. Water and ions are not shown. (**b**) The average separation between the DOPC lipid bilayer and the solid-state surface as a function of time. (**c**) Diffusivity of the DOPC lipids in the plane of the bilayer as a function of the separation between the lipid and the solid-state surface

surface separation of 1.0 nm was assumed at the start of each simulation. Within 15 ns, the DOPC bilayer was seen to make contact with the negatively charged (-1 e/nm^2) surface, followed by complete collapse of the bottom bilayer leaflet by $t=100$ ns, leaving only scattered pockets of interfacial water with a density of ~14 molecules/nm^2. In contrast, the bilayer receded from the positively charged surface at $t=15$ ns and continued receding through to $t=100$ ns. Figure 3b plots the average separation between the DOPC bilayer and the substrate as a function of time for each simulated system. For charge densities of 0 and -1 e/nm^2, the average separation between the DOPC bilayer and the surface diminished rapidly in comparison to positively charged surfaces ($+1$ and $+2$ e/nm^2) which showed a slow increase in lipid–surface separation. The surface charge dependent motion of the bilayer on -1, 0 and $+2$ e/nm^2 surfaces is illustrated in the movies provided in the supplementary material. To verify that these results were robust, the simulations were repeated using different initial conditions, yielding similar results, as shown in supplementary figure 3a. Moreover, three additional simulations showed repulsion of the bilayer from the surface when the surface charge was instantaneously changed from either -1 e/nm^2 or 0 e/nm^2 to $+2$ e/nm^2 during simulations, as shown in supplementary figure 3b.

Our results suggest that the thickness of the hydration layer is dependent on electrostatic interactions between the surface and the DOPC head group. For an isolated DOPC bilayer, the headgroup of the lipid has an electric dipole moment pointing outward from the bilayer surface due to the equilibrium orientation of the positively charged choline group and negatively charged phosphate group (Siu et al. 2008). We calculate a dipole moment of 2.9 ± 0.2 Debye normal to the surface for a DOPC headgroup in an isolated bilayer, in agreement with Siu et al. (Siu et al. 2008). Thus, the bilayer should be attracted to negative surfaces, and repelled from positively charged surfaces, which is consistent with the bilayer motion seen in Fig. 3b. Supplementary figure 3c shows the average electric dipole of the DOPC headgroup along the direction normal to the bilayer. For bilayer-surface separations >0.4 nm, this dipole maintained the isolated value of 2.9 ± 0.2 Debye. For smaller separations, the charge of the surface causes a change in the conformation of the headgroup moieties and, consequently, a change in the electric dipole moment of the headgroup. When the DOPC bilayer was forced <0.3 nm from a positively charged surface, the dipole moment of the headgroup is reversed. This conformational change is likely not energetically favorable and explains the repulsion of the bilayer from the positively charged surface in charge reversal simulations. Interestingly, DOPC bilayers also showed an attraction to neutrally charged surfaces in our simulations.

This is because annealing the model membranes results in the migration of negatively charged oxygen atoms to the surface, giving the neutral surface a surface dipole which in turn electrostatically attracts the bilayer. The simulated surfaces used in these studies do not serve as precise models of experimental SiO_2 and Al_2O_3 surfaces, which would be difficult to create given the lack of knowledge about the atomic structure of the surfaces and their interactions with DOPC lipids. The simulations were intended to show that differences in the surface charge properties of the two materials may be predominantly responsible for differences in hydration layer thickness. The equilibrium separation between an SiO_2 surface and a DOPC bilayer has been reported to be ~1.0 nm (Groves et al. 1997), while our simulations showed a much smaller equilibrium separation. This discrepancy could be due to topographic features of the surface such as surface roughness, affecting the measured separation. Furthermore, the relatively small size of the MD system (105 nm^2) may have suppressed long-range fluctuations of the lipid surface, which would also contribute to a larger measured separation in experiments.

We also investigated the effect of lipid-surface separation on the diffusion kinetics of the lipids in both the upper and lower (nearer to the surface) bilayer leaflets. The diffusivity values were calculated as described in the supplementary information using a protocol similar to Siu et al. (Siu et al. 2008). Figure 3c shows that the lipid diffusivity in the plane of the bilayer increases with increasing lipid-surface separation in all simulations. Both leaflets showed this trend, although the diffusivity was observed to be considerably less in the lower leaflet. These results suggest that DOPC bilayers in equilibrium above a positively charged surface should show higher lipid diffusivities than those above negatively charged surfaces due to a larger lipid-surface separation. Diffusivities of 1.1 ± 0.2 and 6.4 ± 0.8 μm^2/s for lower and upper leaflets were calculated respectively from simulations of the -1 e/nm^2 surface at times >50 ns. For the $+2$ e/nm^2 surface at times >50 ns, we obtained much larger values for these diffusivities: 7.2 ± 2.2 and 11.9 ± 2.5 e/nm^2 respectively. The diffusivity determined here for large lipid-surface separations agree well with previous MD simulations (Siu et al. 2008). Quantitative comparisons between the lipid diffusion coefficients calculated in simulations and those measured in our experiments are complicated by the fact that diffusivity was measured experimentally by observing the motion of TR-DHPE, whose bulky fluorophore likely reduced its diffusivity with respect to the DOPC lipids surrounding it. Differences in the surface roughness of the simulated and experimental surfaces, and the presence of the pore in simulations could also contribute to differences in the measured and simulated diffusivities.
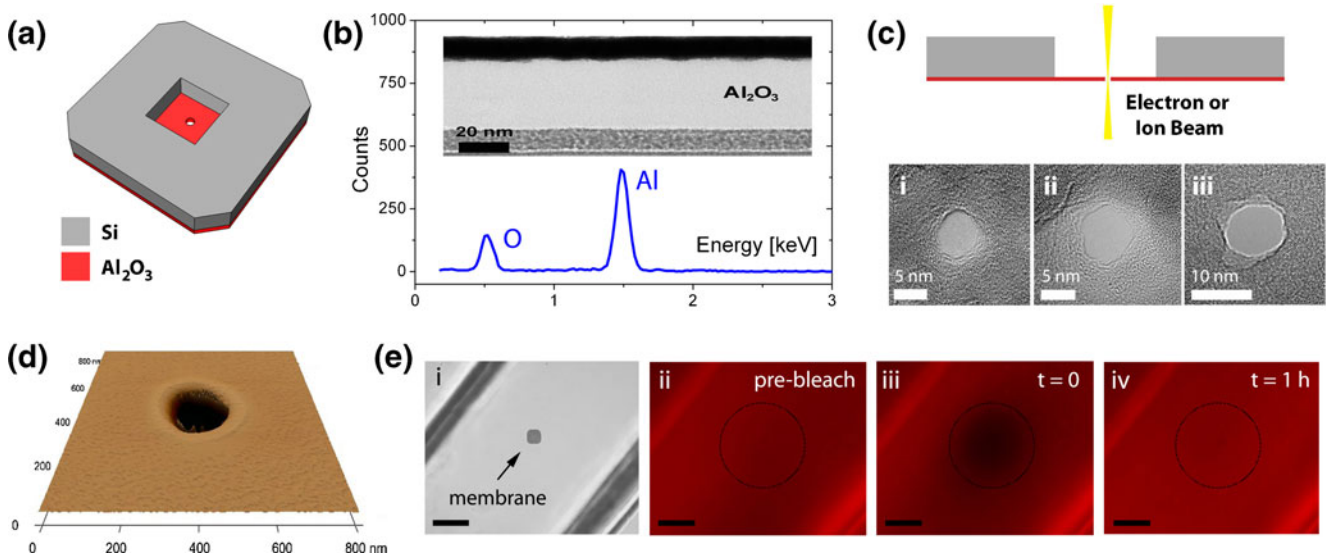
Fig. 4 (**a**) Schematic of a nanopore chip from the backside; The 30×30 μm, 300 μm deep trench in the Si handle layer supports a free-standing Al_2O_3 membrane in which a nanopore is formed (**b**) EDS spectrum from the free-standing membrane confirming the presence of only Al and O (Inset) Cross sectional TEM image of the membrane showing a thickness of 45 ± 5 nm (**c**) Schematic of the nanopore formation process using a convergent electron or ion beam (i–iii) TEM phase contrast images of a 5 nm, 7 nm and 9 nm diameter Al_2O_3 nanopore formed using electron beam based decompositional sputter-ing (**d**) AFM scan of a typical FIB 200 nm pore used in bilayer experiments (**e**) Bilayer integration on solid-state nanopores (100 μm scalebar) (i) Bright field image of a 500 μm wide PDMS channel containing a membrane with a 200 nm nanopore. Fluorescence image after bilayer integration on the nanopore chip (ii) prior to photobleaching the circular target region (iii) immediately after photobleaching (iii) 1 h after photobleaching, showing complete fluorescence recovery

3.4 Al_2O_3 nanopore fabrication and characterization

The solid-state nanopore fabrication process used herein builds on prior work (Venkatesan et al. 2009; Venkatesan et al. 2010). Briefly, a Si support chip containing a single low-stress, mechanically stable 45 ± 5-nm-thick amorphous Al_2O_3 membrane was fabricated using standard micro-fabrication processes as described in the experimental methods. A schematic of the nanopore chip is shown in Fig. 4a. TEM cross sectional analysis and energy dispersive X-ray spectroscopy (EDS) confirmed the thickness and composition (containing only Al and O) of free-standing membranes as shown in Fig. 4b. Nanopores of varying diameter were formed in these Al_2O_3 membranes using a focused electron beam from a JEOL JEM2010F field-emission TEM operated at 197 kV. Figure 4c shows a schematic of the pore formation process along with TEM phase contrast images of 5 nm, 7 nm and 9 nm diameter nanopores used in these experiments. The shot noise in the pore region confirms that the electron beam has completely sputtered through the membrane with the pore quenching in size upon removal of the electron beam. Small Al_2O_3 nanopores formed using this process are well suited for single molecule DNA analysis (Venkatesan et al. 2009; Venkatesan et al. 2010). Larger nanopores were formed in free-standing Al_2O_3 membranes using a FEI DB235 focused ion beam tool. Figure 4d is an AFM scan of a typical ~200 nm pore used in bilayer integration experiments. Post fabrication, nanopore chips were O_2 plasma treated (100 W for 1 min) to render the surface hydrophilic and immediately mounted into a PDMS flow cell into which vesicles were injected and incubated. Figure 4e (i) shows a bright field image of a 500 μm PDMS channel aligned and chemically bonded to an Al_2O_3 nanopore chip containing a single 200 nm nanopore, centered on a 30 μm $\times 30$ μm free-standing membrane. A complete cross-sectional view of the experimental setup is provided in supplementary figure 4a. After vesicle incubation, the surface was perfused using the previously described method (high salt, osmotic pressure and Ca^{2+}) to successfully form a fluid bilayer on the Al_2O_3 nanopore chip. Figure 4e (ii)–(iv) show qualitative FRAP results from the region containing the membrane/nanopore following the perfusion process. The fluorescence recovery observed in the photobleached region confirms the formation of a fluid lipid bilayer over the membrane/nanopore region, consistent with our results on planar Al_2O_3 surfaces. To determine the electrical characteristics of bilayer coated nanopores, ionic current through the pore was measured by placing Ag/AgCl electrodes in each reservoir, with the nanopore forming the only electrical/fluidic connection between the two reservoirs (supplementary figure 4a). The electrical characteristics are discussed in the following section.
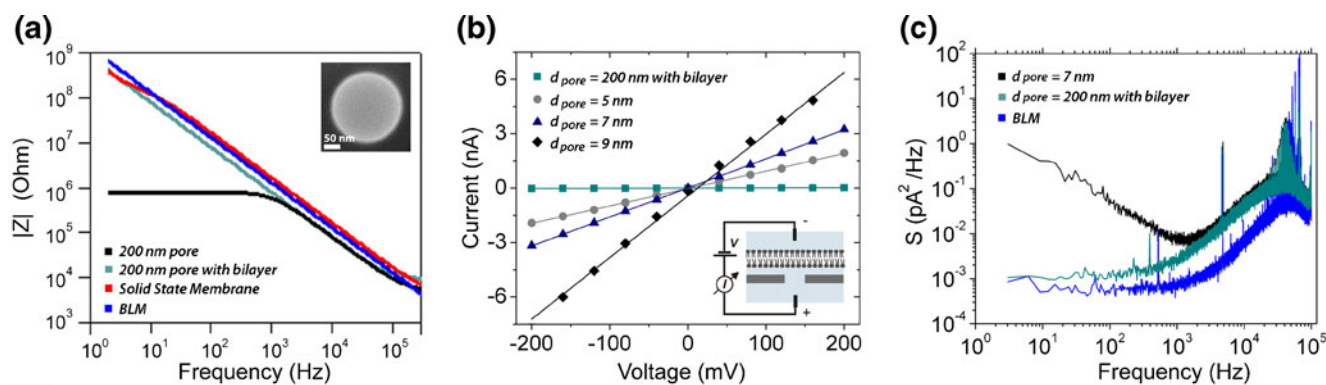
Fig. 5 (a) Impedance spectra from a 200 nm Al_2O_3 nanopore before and after bilayer integration. Following bilayer formation, a $G\Omega$ seal is achieved comparable in magnitude to the impedance of a painted BLM and a solid-state membrane with no pore (Inset) TEM image of the 200 nm pore prior to bilayer formation (b) IV characteristics of a bilayer coated 200 nm Al_2O_3 nanopore ($R=9$ $G\Omega$), relative to uncoated 5 nm ($R=104$ $M\Omega$), 7 nm ($R=62.5$ $M\Omega$) and 9 nm ($R=29.4$ $M\Omega$) diameter nanopores (Inset) Schematic of the DC measurement setup; bilayer formation blocks ion flow through the pore (d) Noise power spectrum from a 7 nm solid-state nanopore showing strong 1/f noise at f<1 kHz. Overlaid are power spectra from a BLM and a bilayer coated Al_2O_3 nanopore. 1/f noise is not observed in either spectra confirming negligible current flow through the bilayer coated nanopore

3.5 Lipid bilayer coated Al_2O_3 nanopore sensors

Monitoring single ion channel activity in lipid bilayers requires a membrane resistance that is in excess of $1G\Omega$. The electrical performance of DOPC bilayers grafted on Al_2O_3 nanopore substrates was characterized using AC impedance spectroscopy and DC current measurements as illustrated in Fig. 5a and b respectively. The impedance of a 200 nm nanopore prior to vesicle fusion and rupture is shown by the black curve of Fig. 5a. Pore resistance in 1 M KCl, 10 mM Tris, pH 8.0 electrolyte is estimated at between several hundred kΩ to 1 MΩ. Following vesicle fusion and rupture, the pore impedance significantly increases into the $G\Omega$ range consistent with the formation of a defect free, pore spanning lipid bilayer. Figure 5a also compares the impedance of a bilayer grafted Al_2O_3 nanopore sensor with the impedance of traditional painted BLMs and solid state membranes containing no nanopore. The impedance of all three systems is comparable and in the $G\Omega$ range. DC measurements revealed a resistance of ~9 $G\Omega$ for bilayer grafted Al_2O_3 nanopores in comparison to BLM and solid-state membrane resistances of 19 $G\Omega$ and 13 $G\Omega$ respectively (supplementary figure 4b). These values are in good agreement with impedance spectra from DPhPC supported bilayers formed on AAO templates (Han et al. 2007) and nano-BLMs formed using the painting method on functionalized gold coated AAO substrates (Romer and Steinem 2004). An order of magnitude improvement in bilayer resistance is observed over bilayers formed through vesicle fusion on mercaptan coated gold surfaces (Stelzle et al. 1993). The authors accredit the low bilayer resistance on mercaptan coated gold to incomplete surface coverage and bilayer defects during vesicle fusion. These defects were not observed in

bilayers formed on Al_2O_3 at high vesicle concentrations, likely due to the formation of a high density SVL prior to the transition to a supported bilayer.
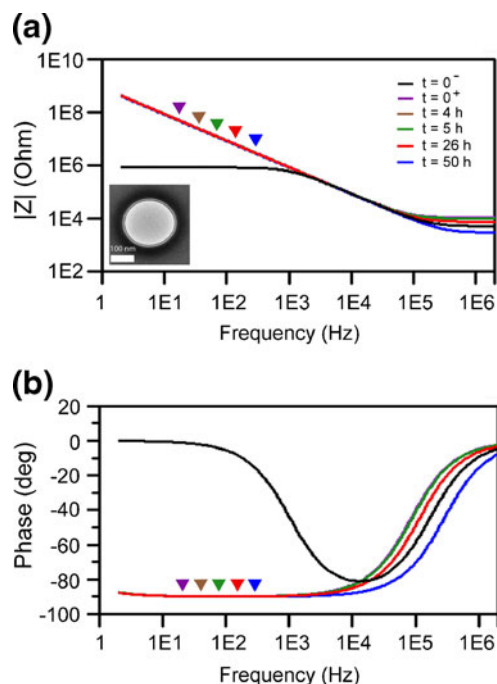

Fig. 6 Stability of bilayer coated Al_2O_3 nanopores as a function of time; Impedance (a) magnitude and (b) phase. Prior to bilayer formation ($t=0^-$), resistive behavior is observed (resistance of 800 kΩ and phase of 0°) at low frequencies, consistent with an open pore. Following bilayer formation ($t=0^+$), capacitive behavior is observed ($G\Omega$ resistance and phase of $-90°$ at low frequencies), confirming the formation of an electrically insulating bilayer membrane on the 200 nm nanopore. High pore impedance was maintained for over 50 h, confirming the stability of this hybrid biological/solid state membrane (Inset) TEM phase contrast image of a typical 200 nm pore used in bilayer integration experiments

Figure 5b overlays the current–voltage (IV) characteristics of open 5 nm, 7 nm and 9 nm diameter Al_2O_3 solid-state nanopores (pore resistances of 104 MΩ, 62.5 MΩ and 29.4 MΩ respectively), with the IV characteristics of a 200 nm diameter Al_2O_3 nanopore supporting a fluid DOPC bilayer (resistance of 9 GΩ). The fluid DOPC bilayer prevents ion transport through the 200 nm diameter Al_2O_3 nanopore, resulting in an ionic current that is orders of magnitude less than that observed through even a small, 5 nm Al_2O_3 nanopore. Exclusively large ~200 nm pores were used in bilayer formation experiments for two reasons; (1) to rule out any possibility of pore clogging with lipid molecules (biomolecule clogging is observed during DNA or protein translocation experiments through very small Al_2O_3 nanopores) and, (2) to maximize the probability of membrane protein insertion in experiments seeking to incorporate α-hemolysin. Figure 5c illustrates a typical noise power spectrum from a ~7 nm nanopore showing strong low frequency 1/f noise characteristics. 1/f noise in solid state nanopores is attributed to two mechanisms, fluctuations in the total number of charge carriers (ions) through the nanopore (Smeets et al. 2009) and fluctuations in ion mobility due to electrostatic trapping at surface sites (Hoogerheide et al. 2009). As expected in the case of a BLM, low frequency 1/f noise is not observed as the membrane is impermeable to ions. Interestingly, 1/f noise is also not observed in current measurements through a bilayer spanning Al_2O_3 nanopore. This is again due to negligible ion flow across the hybrid biological/solid-state membrane, further confirming the formation of a high impedance seal.

3.6 Stability of bilayer coated Al_2O_3 nanopores

The suitability of classical BLMs in biosensor applications is limited by their short lifetimes (typically 6–10 h), beyond which membrane rupture occurs. BLMs are also highly susceptible to mechanical shock and thermal fluctuations. The need for robust BLMs is most evident in biological nanopore based DNA sequencing approaches that require substantial membrane stability to achieve long read lengths (Clarke et al. 2009; Derrington et al. 2010). The DOPC bilayers formed in these experiments on single Al_2O_3 nanopores show excellent bilayer stability as illustrated in Fig. 6. GΩ impedances are maintained for over 50 h as verified from the magnitude and phase plots of Fig. 6a and b respectively.

Prior to bilayer formation on the nanopore ($t=0^-$ hr), we observe a pore resistance of ~800 kΩ and a phase of 0° for f<1 kHz, corresponding to the typical resistive behavior of a nanopore. Following the vesicle fusion and rupture process on the Al_2O_3 nanopore, at $t=0^+$ hr, a clear shift in the magnitude and phase spectra is seen. The GΩ

impedance and −90° phase shift near DC, signifies capacitive behavior corresponding to the formation of an electrically insulating, fluid bilayer. This capacitive behavior is maintained for over 50 h and is comparable to the state-of-the-art in supported bilayers, more specifically, nano-BLMs that are capable of maintaining GΩ seals for over 30 h (Romer and Steinem 2004) and POPC supported bilayers formed on functionalized AAO templates that are stable for over 50 h (Han et al. 2007).

4 Conclusions

This work presents the formation of highly fluid, defect free lipid bilayers on unmodified Al_2O_3 surfaces through vesicle fusion and applies this methodology to form high impedance, mobile bilayers on single Al_2O_3 nanopore sensors. Lipid bilayer formation on Al_2O_3 occurs exclusively in the presence of Ca^{2+} and high osmotic pressure, resulting in bilayers that exhibit significantly higher lateral fluidity than those formed on planar SiO_2 and TiO_2 substrates. Molecular dynamics simulations attribute the greater fluidity to a larger separation between the DOPC bilayer and the Al_2O_3 surface, which is in turn due to electrostatic repulsion between the headgroups of DOPC and the positively charged surface. AFM imaging has independently confirmed a 1.5–2.0 nm separation between the bilayer and Al_2O_3 surface. These results suggest that bilayer coated Al_2O_3 surfaces may be well suited for supporting membrane proteins, the thick interfacial water layer on Al_2O_3 permitting the integration of a broader range of membrane active peptides, whilst helping reduce protein immobilization and denaturation through surface contact. In the pharmaceutical and medical industries, such a platform would facilitate the screening of drugs specific to a broader range of membrane proteins in their native environment. Furthermore, lipid bilayers formed on Al_2O_3 nanopore sensors exhibit all the advantages of conventional BLMs and supported bilayers formed on SiO_2 (simple to form, GΩ electrical seals), but also exhibit enhanced mechanical stability (stable for over 50 h) and increased fluidity relative to their supported bilayer counterparts. The bilayer integrated solid-state membrane platform reported in this work, provides an important first step in the development of a hybrid biological solid-state nanopore. By integrating chemically selective ion channels and biological nanopores into this platform, this technology could find widespread use in medical diagnostics, drug screening and in next generation DNA sequencing.

References

S.P. Adiga, P. Zapol, L.A. Curtiss, J. Phys. Chem. C **111**(20), 7422–7429 (2007)

A. Aksimentiev, Nanoscale **2**(4), 468–483 (2010)

H.C. Andersen, J. Comput. Phys. **52**(1), 24–34 (1983)

D. Axelrod, D.E. Koppel, J. Schlessinger, E. Elson, W.W. Webb, Biophys. J. **16**(9), 1055–1069 (1976)

P.F. Batcho, D.A. Case, T. Schlick, J. Chem. Phys. **115**(9), 4003–4018 (2001)

A. Berquand, P.E. Mazeran, J. Pantigny, V. Proux-Delrouyre, J.M. Laval, C. Bourdillon, Langmuir **19**(5), 1700–1707 (2003)

T. Cassier, A. Sinner, A. Offenhauser, H. Mohwald, Colloids Surf. B **15**(3–4), 215–225 (1999)

E. Castellana, P. Cremer, Surf. Sci. Rep. **61**(10), 429–444 (2006)

T. Cha, A. Guo, X.Y. Zhu, Biophys. J. **90**(4), 1270–1274 (2006)

H. Chang, B. Venkatesan, S. Iqbal, G. Andreadakis, F. Kosari, G. Vasmatzis, D. Peroulis, R. Bashir, Biomed. Microdevices **8**(3), 263–269 (2006)

J. Clarke, H.C. Wu, L. Jayasinghe, A. Patel, S. Reid, H. Bayley, Nat. Nanotechnol. **4**(4), 265–270 (2009)

P.S. Cremer, S.G. Boxer, J. Phys. Chem. B **103**(13), 2554–2559 (1999)

E.R. Cruz-Chu, A. Aksimentiev, K. Schulten, J. Phys. Chem. B **110** (43), 21497–21508 (2006)

G. Csucs, J.J. Ramsden, Biochim. Et Biophys. Acta Biomembr. **1369** (1), 61–70 (1998)

I.M. Derrington, T.Z. Butler, M.D. Collins, E. Manrao, M. Pavlenok, M. Niederweis, J.H. Gundlach, Proc. Natl Acad. Sci. **107**(37), 16060–16065 (2010)

J. Drews, Science **287**(5460), 1960–1964 (2000)

J. Drexler, C. Steinem, J. Phys. Chem. B **107**(40), 11245–11254 (2003)

H.C. Gaede, K.M. Luckett, I.V. Polozov, K. Gawrisch, Langmuir **20** (18), 7711–7719 (2004)

A. Grakoui, S.K. Bromley, C. Sumen, M.M. Davis, A.S. Shaw, P.M. Allen, M.L. Dustin, Science **285**(5425), 221–227 (1999)

J.T. Groves, L.K. Mahal, C.R. Bertozzi, Langmuir **17**(17), 5129–5133 (2001)

J.T. Groves, N. Ulman, S.G. Boxer, Science **275**(5300), 651–653 (1997)

J.T. Groves, N. Ulman, P.S. Cremer, S.G. Boxer, Langmuir **14**(12), 3347–3350 (1998)

X.J. Han, A. Studer, H. Sehr, I. Geissbuhler, M. Di Berardino, F.K. Winkler, L.X. Tiefenauer, Adv. Mater. **19**(24), 4466 (2007)

J.B. Heng, A. Aksimentiev, C. Ho, P. Marks, Y.V. Grinkova, S. Sligar, K. Schulten, G. Timp, Nano Lett. **5**(10), 1883–1888 (2005)

D.P. Hoogerheide, S. Garaj, J.A. Golovchenko, Phys. Rev. Lett. **102** (25), 256804 (2009)

S.J. Johnson, T.M. Bayerl, D.C. McDermott, G.W. Adam, A.R. Rennie, R.K. Thomas, E. Sackmann, Biophys. J. **59**(2), 289–294 (1991)

H.G. Kapitza, G. Mcgregor, K.A. Jacobson, Proc. Natl Acad. Sci. U.S. A. **82**(12), 4122–4126 (1985)

C. Kataoka-Hamai, H. Inoue, Y. Miyahara, Langmuir **24**(17), 9916–9920 (2008)

B.W. Koenig, S. Krueger, W.J. Orts, C.F. Majkrzak, N.F. Berk, J. V. Silverton, K. Gawrisch, Langmuir **12**(5), 1343–1350 (1996)

S. Kumar, J.H. Hoh, Langmuir **16**(25), 9936–9940 (2000)

Z.V. Leonenko, D. Merkle, S.P. Lees-Miller, D.T. Cramb, Langmuir **18**(12), 4873–4884 (2002)

J. Li, M. Gershow, D. Stein, E. Brandin, J.A. Golovchenko, Nat. Mater. **2**(9), 611–615 (2003)

A.D. MacKerell, A.D. MacKerell, D. Bashford, M. Bellott, R.L. Dunbrack, J.D. Evanseck, M.J. Field, S. Fischer, J. Gao, H. Guo, S. Ha, D. Joseph-McCarthy, L. Kuchnir, K. Kuczera, F.T.K. Lau, C. Mattos, S. Michnick, T. Ngo, D.T. Nguyen, B. Prodhom, W.E. Reiher, B. Roux, M. Schlenkrich, J.C. Smith, R. Stote, J. Straub, M. Watanabe, J. Wiorkiewicz-Kuczera, D. Yin, M. Karplus, J. Phys. Chem. B **102**(18), 3586–3616 (1998)

M.D. Mager, B. Almquist, N.A. Melosh, Langmuir **24**(22), 12734–12737 (2008)

M.D. Mager, N.A. Melosh, Adv. Mater. **20**(23), 4423–4427 (2008)

G.J. Martyna, D.J. Tobias, M.L. Klein, J. Chem. Phys. **101**(5), 4177–4189 (1994)

B. McNally, M. Wanunu and A. Meller, Nano Lett. (2008)

S. Miyamoto, P.A. Kollman, J. Comput. Chem. **13**(8), 952–962 (1992)

P. Nollert, H. Kiefer, F. Jahnig, Biophys. J. **69**(4), 1447–1455 (1995)

J.C. Phillips, R. Braun, W. Wang, J. Gumbart, E. Tajkhorshid, E. Villa, C. Chipot, R.D. Skeel, L. Kalé, K. Schulten, J. Comput. Chem. **26**(16), 1781–1802 (2005)

J. Raedler, H. Strey, E. Sackmann, Langmuir **11**(11), 4539–4548 (1995)

E. Reimhult, F. Hook, B. Kasemo, J. Chem. Phys. **117**(16), 7401–7404 (2002)

E. Reimhult, F. Hook, B. Kasemo, Langmuir **19**(5), 1681–1691 (2003)

R. Richter, A. Mukhopadhyay, A. Brisson, Biophys. J. **85**(5), 3035–3047 (2003)

W. Romer, C. Steinem, Biophys. J. **86**(2), 955–965 (2004)

R.F. Roskamp, I.K. Vockenroth, N. Eisenmenger, J. Braunagel, I. Koper, Chemphyschem **9**(13), 1920–1924 (2008)

E. Sackmann, Science **271**(5245), 43–48 (1996)

J. Shi, T. Yang, S. Kataoka, Y. Zhang, A.J. Diaz, P.S. Cremer, J. Am. Chem. Soc. **129**(18), 5954–5961 (2007)

S.W.I. Siu, R. Vacha, P. Jungwirth, R.A. Bockmann, J. Chem. Phys. **128**(12), 125103–12 (2008)

R.M.M. Smeets, N.H. Dekker, C. Dekker, Nanotechnology **20**(9), 095501 (2009)

R.M.M. Smeets, S.W. Kowalczyk, A.R. Hall, N.H. Dekker and C. Dekker, Nano Lett. (2008)

J.M. Solletti, M. Botreau, F. Sommer, W.L. Brunat, S. Kasas, T.M. Duc, M.R. Celio, Langmuir **12**(22), 5379–5386 (1996)

T.E. Starr, N.L. Thompson, Langmuir **16**(26), 10301–10308 (2000)

M. Stelzle, G. Weissmuller, E. Sackmann, J. Phys. Chem. **97**(12), 2974–2981 (1993)

A.J. Storm, C. Storm, J. Chen, H. Zandbergen, J.-F. Joanny, C. Dekker, Nano Lett. **5**(7), 1193–1197 (2005)

B.M. Venkatesan, B. Dorvel, S. Yemenicioglu, N. Watkins, I. Petrov, R. Bashir, Adv. Mater. **21**(27), 2771–2776 (2009)

B.M. Venkatesan, A.B. Shah, J.M. Zuo, R. Bashir, Adv. Funct. Mater. **20**(8), 1266–1275 (2010)

R.J. White, B. Zhang, S. Daniel, J.M. Tang, E.N. Ervin, P.S. Cremer, H.S. White, Langmuir **22**(25), 10777–10783 (2006)

Q. Zhao, J. Comer, V. Dimitrov, S. Yemenicioglu, A. Aksimentiev, G. Timp, Nucleic Acids Res. **36**(5), 1532–1541 (2008)